

Hydrogen Effects on the Spall Strength and Fracture Characteristics of Amorphous Fe-Si-B Alloy at Very High Strain Rates

N. ELIAZ, E. MOSHE, S. ELIEZER, and D. ELIEZER

A novel approach is suggested, using laser-induced shock wave measurements to estimate the effects of cathodic hydrogen charging on the mechanical properties and fracture characteristics of materials. This approach is applied to (1) determine the dominant mechanism of hydrogen embrittlement (HE) in an amorphous $\text{Fe}_{80}\text{B}_{11}\text{Si}_9$ alloy; and (2) estimate the effects of the high pressures involved in cathodic charging. The dynamic spall strength of an amorphous $\text{Fe}_{80}\text{B}_{11}\text{Si}_9$ alloy shocked before and after hydrogenation by a high-power laser to very high pressures (tens of giga Pascals) is measured. The dynamic spall strength of crystalline iron is measured as well for comparison. An optically recording velocity interferometer system (ORVIS) is used to measure the profile of the free surface velocity in time. The spall strength and the strain rate are calculated from the measurement of the free surface velocity as a function of time. Fracture characteristics are studied by scanning electron microscopy (SEM). The main conclusions are (1) the most reasonable mechanism of HE in the amorphous Fe-Si-B alloy is the high-pressure bubble formation; (2) the high pressures involved in cathodic hydrogen charging or laser-induced shock waves measurements may have similar effects on fracture characteristics; and (3) at very high strain rates, the spall strength is determined mainly by the interatomic bonds.

I. INTRODUCTION

MATERIAL behavior under conditions of high strain rates is of practical importance in such problems as the response of structures to blast and impulsive loads, contact stresses under high-speed bearings, high-speed machining, explosive forming, and ballistics. The spectrum of strain rates under various conditions and tests is summarized in Table I. Shock-wave propagation through a thin plate is essentially one-dimensional in the direction of the shock front. For small plastic strains, this produces a state of near triaxial loading. Thus, shock loading provides an environment for subjecting materials to high stresses without corresponding large plastic deformations. There are marked differences between fracture under impulsive loads and under static loads. For example, with impulsive loads, there is no time for the stress to be distributed throughout the entire body so that fracture can occur in one part of the solid independently of what happens in another part.^[1]

When a high-power laser pulse irradiates a metal foil it creates a high-temperature and high-pressure plasma layer in it, which then expands perpendicularly to the foil. The expanding plasma induces a shock wave in the target, moving toward the free (rear) surface. When the shock wave reaches the free surface, the latter is accelerated to a velocity u_{fs} , and the former is reflected as a rarefaction wave. The rarefaction wave, moving in an opposite direction, causes

deceleration of the free surface. The two rarefaction waves (the tail of the initial pressure wave and the wave reflected from the free surface), running in opposite directions, generate tension of the material with an amplitude that increases with the distance from the rear surface and with time. When the tension exceeds the material strength, a spall forms in a plane parallel to the rear surface.^[2,3] The spall may be defined as the process of internal failure or rupture of condensed media due to stresses in excess of the tensile strength of the material. As a result of the material expansion from the spall area outside, a second pressure wave is formed, which then moves in the direction of the initial shock wave and accelerates the free surface. This second pressure wave is reflected from the free surface as a rarefaction wave. The reverberations of the waves in the spall region accelerate and decelerate the free surface alternately until they decay due to dissipation losses. The spall pressure or the spall strength of the material may be determined by measurement of the free surface velocity history. An ideal free surface velocity profile in time is shown in Figure 1. In the acoustic approximation, the shock and rarefaction waves are considered weak so that their velocities are equal to the sound velocity. Therefore, time point 4 is the mean of times at the maximum and first minimum of the free surface velocity (time points 3 and 5, respectively). The spatial coordinate of the spall plane is the distance the waves travel during that time.

An ORVIS^[4,5,6] is used in this work to measure the time evolution of the free surface. This diagnostic method provides an accurate continuous measurement of the surface velocity with a very high time resolution (up to tens of picoseconds). It also has the advantages of being noninterfering with the motion of the shocked target and being applicable to very thin samples (such as ribbons). A short and tunable laser pulse duration implies a higher strain rate than

N. ELIAZ, formerly Ph.D. Student at the Department of Materials Engineering, Ben-Gurion University of the Negev, is Postdoctoral Fellow, H.H. Uhlig Corrosion Laboratory, Massachusetts Institute of Technology, Cambridge, MA 02139. E. MOSHE, Researcher, and S. ELIEZER, Professor, are with the Department of Plasma Physics, Soreq NRC, Yavne 81800, Israel. D. ELIEZER, Professor, is with the Department of Materials Engineering, Ben-Gurion University of the Negev, Beer-Sheva 84105, Israel.

Manuscript submitted July 15, 1999.

Table I. Spectrum of Strain Rates under Various Conditions and Tests

Range of Strain Rate (s^{-1})	Condition or Test Type
10^{-8} to 10^{-5}	creep tests at constant load or stress
10^{-5} to 10^{-1}	static tension tests with hydraulic or screw-driven machines
10^{-1} to 10^2	dynamic tension or compression tests
10^2 to 10^4	high-speed testing using impact bars
10^4 to 10^8	hypervelocity impact using gas guns or explosively driven projectiles (shock-wave propagation)

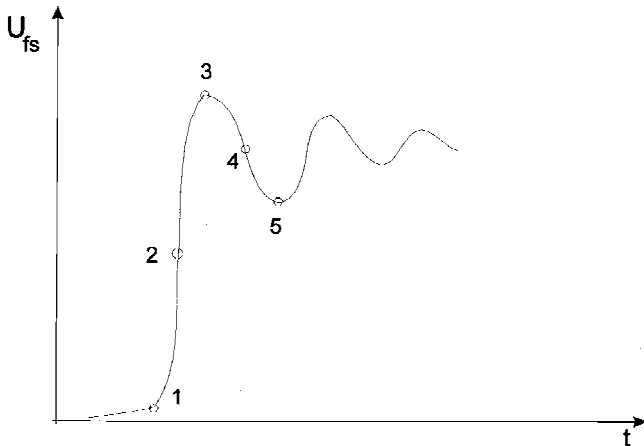


Fig. 1—An ideal free surface velocity profile in time. 1—arrival of the first shock wave very close to the rear surface, 2—peak of the shock wave, 3—beginning of deceleration of the rear surface by rarefaction wave, 4—spall formation, and 5—beginning of acceleration due to second shock wave.

in impact experiments and the possibility of studying high-pressure time-dependent phenomena.

It has long been recognized that hydrogen might embrittle many crystalline metals and alloys. The embrittlement is manifested by the nonductile fracture mode, reduced ductility, and reduced tensile strength. Several mechanisms have been proposed to explain hydrogen embrittlement (HE) in crystalline materials. The most common ones are the high-pressure bubble formation,^[7] reduction in surface energy (adsorption mechanism),^[8] reduction in the lattice cohesive force (decohesion mechanism),^[9] hydrogen interaction with dislocations,^[10–14] and hydride formation.^[15,16]

Due to their metallic bonding and the lack of long-range order, amorphous alloys are characterized by unique mechanical, magnetic, electrical, and environmental properties.^[17–21] Nevertheless, some metallic glasses are susceptible to HE. Because amorphous alloys are distinguished from crystalline alloys in their deformation behavior (*e.g.*, dislocations are absent, and fracture occurs immediately after the elastic region), the embrittlement mechanisms in amorphous alloys may be different from those in the crystalline counterparts. The study of HE is of significant importance for many applications of metallic glasses. In addition, it may also be useful for understanding the deformation and fracture mechanisms of metallic glasses in more detail. The effects of hydrogen on the mechanical properties and fracture characteristics of metallic glasses have been reported extensively (see, for example, References 22 through 28). Eliaz and Eliezer have recently published^[29] a comprehensive review of hydrogen interaction with amorphous alloys.

In the framework of investigating hydrogen interaction

with amorphous alloys, HE of amorphous $Fe_{80}B_{11}Si_9$ has been studied in detail.^[28,30] On the one hand, a study of the embrittlement phenomenon in this alloy is complicated because neither changes in microhardness nor Palmqvist, radial, or median cracks in the microindentation region are observed after hydrogenation (though macroscopically, it is clear that the material has become significantly brittle). The former behavior may be due to the low solubility of hydrogen in this alloy, whereas the latter may be due to the very low loads applied on the thin ribbon. In addition, tensile tests of brittle materials and thin ribbons require many samples and are involved with many technical problems. On the other hand, microscopic results^[28] and calculation^[30] of an effective activation energy of hydrogen detrapping, $E_{aT} = 31.84 \pm 5.79 \text{ kJ mol}^{-1}$, which is similar to the one reported for hydrogen trapping in microvoids in crystalline metals ($37.63 \text{ kJ mol}^{-1}$),^[31] support the mechanism of high-pressure bubble formation.

In this article, we suggest a novel approach for estimating the effects of cathodic hydrogen charging on the mechanical properties and fracture characteristics of amorphous materials in the shape of thin ribbons. This approach is applied to determine the dominant mechanism of HE in an amorphous $Fe_{80}B_{11}Si_9$ alloy and to estimate the effects of the high pressures involved in cathodic charging. We measure the dynamic spall strength of an amorphous $Fe_{80}B_{11}Si_9$ alloy shocked before and after hydrogenation by a high-power laser to very high pressures (tens of giga Pascals). The dynamic spall strength of crystalline iron is measured as well for comparison. Such measurements may make it easier to determine the dominant mechanism of HE because they make it possible to distinguish between mechanisms that are strain rate dependent (*e.g.*, dislocations movement in crystalline metals or crack propagation) and mechanisms that are relatively independent on the strain rate (*e.g.*, decohesion).

II. EXPERIMENTAL

In this research, we use ribbons of amorphous $Fe_{80}B_{11}Si_9$ (Metglas 2605SA1; thickness, t , of about $25 \mu\text{m}$) produced by planar flow casting and kindly supplied by AlliedSignal Inc. (Parsippany, NJ). For comparison, several experiments were conducted with targets of pure (99.5 pct) crystalline iron (Goodfellow, Cambridge, UK, $t \sim 50 \mu\text{m}$).

The experimental setup for the free surface velocity measurements was described in References 6, 32, and 33 and is shown in Figure 2. The main laser system that generates the shock waves is based on a NY-60 Nd:YAG oscillator followed by two glass amplifiers. The laser operates at a wavelength of $1.06 \mu\text{m}$, a pulse width (full-width at half-maximum (FWHM)) of 2 to 7 ns, and energy in the range of 10 to 100 J and is focused to a spot diameter in the range

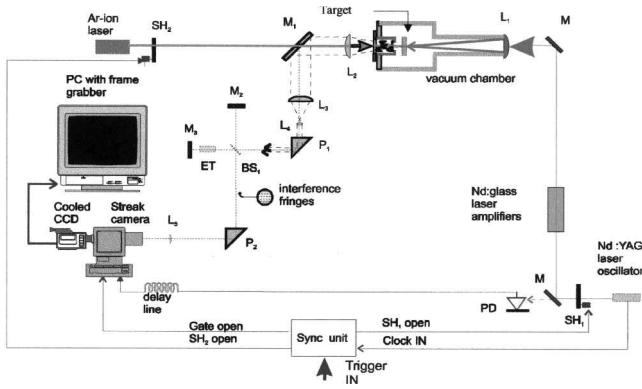


Fig. 2—Schematic description of the ORVIS and the laser-induced shock waves experiment. M_1 , M_2 , M_3 —mirrors; L_1 , L_2 , L_3 , L_4 , L_5 —lenses; BS_1 , BS_2 —beam splitters; ET —etalon; P_1 , P_2 —prisms; SH_1 , SH_2 —shutters; and PD —photodiodes.

of 200 to 600 μm . The laser irradiance in the experiments reported herein is $5 \cdot 10^{11}$ to $5 \cdot 10^{13} \text{ W cm}^{-2}$. The diagnostic interferometric system consists of a continuous argon-ion laser focused to 50 μm on the rear surface, aligned accurately with the spot of the main laser beam. The light reflected from the moving free surface undergoes a Doppler shift proportional to the velocity of the free surface. The light is collected, collimated and reflected into a Michelson interferometer. A beam splitter divides the beam into two nonequal legs. An etalon is placed in the route of one of the legs. The two beams are back reflected and then recombine. The recombination of the two beams produces an interference pattern of parallel fringes. These fringes are generated from light that was reflected from the target at two different times. Therefore, when the target is moving, the fringes are shifted. The interference pattern is imaged by a cylindrical lens to a set of bright spots on the entrance slit of a streak camera. The cylindrical lens is used to increase the interference pattern intensity at the camera entrance slit. The interference pattern is analyzed with an image processing system including a cool CCD camera, a frame grabber, and a PC. The picture consisting of 512×512 pixels is digitized using the MATLAB image processing toolbox.

Due to the very short pulse duration (several nanoseconds) and the rapid time of high pressure formation (1 ns), a very high strain rate (of the order of 10^7 s^{-1}) is obtained in the target. In addition, if the diameter of the laser spot is one order of magnitude larger than the target thickness, one may speak about one-dimensional geometry of the shock waves propagating through the target.

Cathodic hydrogen charging of amorphous Fe-Si-B ribbons was performed for 30 minutes at 100 A m^{-2} in a solution of $0.1 \text{ N H}_2\text{SO}_4$ with $5 \text{ mg L}^{-1} \text{ NaAsO}_2$ as a surface poison. The fracture morphology was studied by means of scanning electron microscopy (SEM). Static tensile tests under strain rates of about 10^{-4} s^{-1} were conducted as well for comparison.

III. CALCULATION CONCEPT

The velocity history of the moving free surface is determined from the change in the interference pattern. All calculations are performed on the basis of this interference pattern.

The spall strength is measured vs strain rate. The spall pressure is calculated from measurements of the dependence of free surface on time using the acoustic approximation. The time dependence of the pressure inside the target may be calculated by summation of the motion equations describing the interaction between two rarefaction waves.

The law of momentum conservation may express the free surface velocity

$$u_{fs} = 2u_p \quad [1]$$

where u_p is the particle velocity (mass velocity in the shocked material).

The fringes move in a direction perpendicular to their orientation when the velocity changes, with the direction depending on the sign of the velocity change. The velocity of the moving surface is related to the vertical position, $y(t)$, of the interference pattern as a function of time:^[4,34,35]

$$u_{fs}(t) = \frac{\lambda c}{4L_e \left(n - \frac{1}{n} \right)} \cdot \frac{y(t)}{(1 + \delta)d} \quad [2]$$

where λ is the diagnostic laser wavelength, d is the fringe spacing, L_e is the length of the etalon, n is its index of refraction, c is the speed of light in vacuum, and $(1 + \delta)$ is a correction term due to the wavelength dependence of the refractive index of the etalon material. In the experiments herein, $\delta = 0.034$ at the argon laser wavelength of 514.5 nm.

The spall strength may be expressed by

$$P_{\text{spall}} = \frac{1}{2} \rho c_s (u_{\text{max}} - u_{\text{min}}) \quad [3]$$

where ρ is the initial density of target material, c_s is the sound velocity, u_{max} is the peak velocity of the free surface, and u_{min} is the velocity at the first minimum of the free surface profile. The sound velocity in the amorphous alloy is taken from Kaczkowski and Nam ($\sim 4 \text{ km s}^{-1}$ for amorphous $\text{Fe}_{78}\text{B}_{12}\text{Si}_{10}$).^[36]

The strain rate is calculated in each experiment from the slope of the profile in the spall region:

$$\dot{\varepsilon} = \left. \frac{du_{fs}}{dt} \right|_{t = t_{\text{spall}}} \cdot \frac{1}{2c_s} \quad [4]$$

IV. RESULTS AND DISCUSSION

The results of experiments with either as-received or hydrogenated amorphous samples are summarized in Table II. Because the thickness of the target is only 25 μm , and the shock wave velocity in the target is slightly higher than the sound velocity, a 7-ns-wide laser pulse continues to create pressure while the shock wave is already approaching the free surface. The measured free surface velocity in this case is the sum of an accelerated mass center velocity and the reverberations of the free surface relative to the mass center. Therefore, in order to find the real velocity change, one should subtract the mass center velocity from the measured free surface velocity:

$$\Delta u_m = \Delta u_{fs} - a_m \Delta t \quad [5]$$

where Δu_m is the real difference between velocities relative to the mass center, Δu_{fs} is the difference between the peak

Table II. Summary of Laser-Induced Shock Wave Measurements in Uncharged as well as Hydrogenated Amorphous Fe₈₀B₁₁Si₉ Alloy and in Uncharged Crystalline Iron

Material	P_{spall} (GPa)	ϵ (s ⁻¹)	FWHM (ns)
Uncharged amorphous Fe ₈₀ B ₁₁ Si ₉	-5.70 ± 0.23	3.0 · 10 ⁷	2.2*
	-3.50 ± 0.18	1.8 · 10 ⁷	2.2*
	-2.80 ± 0.22	1.0 · 10 ⁷	7**
Hydrogenated amorphous Fe ₈₀ B ₁₁ Si ₉	-3.15 ± 0.25	1.4 · 10 ⁷	7**
Uncharged crystalline Fe	-1.90 ± 0.15	3.5 · 10 ⁶	2.2*

* Without acceleration.

** With acceleration.

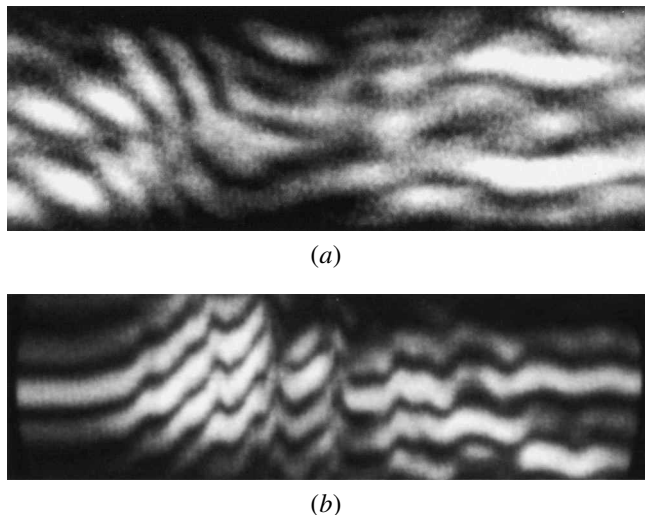


Fig. 3—The interference pattern of uncharged amorphous Fe-Si-B alloy, obtained with ORVIS in experiments (b) with or (a) without acceleration while reverberation.

and the first minimum in the profile of free surface velocity, a_m is the acceleration of the mass center, and Δt is the time between the peak and the first minimum.

It is known that the spall strength depends on the strain rate. Indeed, in Table II, one can see that high strength values of 3.5 and 5.7 GPa are measured under conditions of high strain rates of $1.8 \cdot 10^7$ and $3.0 \cdot 10^7$ s⁻¹, respectively. It should be noted that under static tensile tests at strain rates of $\sim 10^{-4}$ s⁻¹, we measured a fracture strength of 1.23 GPa (125 kg mm⁻²) for the as-received amorphous alloy. This value is similar to the ones reported elsewhere for iron- and iron-nickel-based amorphous alloys under similar test conditions.^[37,38] The similar values of the spall strength of the amorphous alloy at low and at high strain rates may indicate that in both cases, failure development is influenced by similar factors.

In the case of the hydrogenated alloy, an average spall strength of 3.15 GPa was measured at a strain rate of $1.4 \cdot 10^7$ s⁻¹. The spall strength of the hydrogenated amorphous alloy is, thus, approximately equal to that of the uncharged alloy taking into account the effect of strain rate on strength and the measurement error.

The interference patterns of the uncharged amorphous alloy obtained with ORVIS in experiments with (b) or without (a) acceleration while reverberation are presented in Figure 3. The time scale in this figure increases from left to right up to 5.6 ns. The free surface velocity is related to

the vertical position on the interference pattern vs time, and the distance between two fringes (the fringe constant) is 0.301 km s^{-1} . The fringes are parallel to the time axis before the free surface undergoes acceleration. Then the fringe pattern starts shifting, indicating the acceleration of the free surface. It can be seen that the fringes are not parallel to one another (sometimes they are even mixed). This behavior indicates the disorder in the amorphous structure and results from material motion in different directions and at different velocities. The conversion of the interference patterns from Figure 3 to dimensions of free surface velocity vs time was performed by MATLAB and is presented in Figure 4.

Figure 5 presents SEM micrographs from the region of the penetrating hole, which was formed after the severance of the spall layer in the uncharged amorphous alloy (laser pulse energy is 26 J, laser width is 2.2 ns). Macroscopically (Figure 5 (a)), the shape of the hole is starlike with secondary cracks propagating from the edge of each arm. Such a starlike shape has not been observed in the dynamic failure of crystalline metals and may result either from unique properties of the amorphous structure or from macroscopic embrittlement. Because similar fracture shapes were observed in ordinary glasses (see, for example, Reference 39), we believe that this starlike shape is related to the amorphous structure. Furthermore, when a crack is formed in ductile metals, part of the energy is absorbed in the material as plastic deformation, thus, preventing the propagation of secondary cracks. On the other hand, the absence of dislocations in amorphous metals prevents significant plastic deformation before fracture, thus, the chance for propagation of secondary cracks increases. Figure 5(b) presents a typical fracture surface from the hole region. One can notice the vein pattern typical to fracture of amorphous metals by inhomogeneous flow. The front surface of the sample is noticed as well. Due to the ablation (emission of hot material) and hot temperature, a crater is formed on this surface, around which a molten material is splashed. The splashed material quickly solidifies, as can be seen from the surface topography. In a small region of the fracture surface, a cellular pattern was observed (Figure 5(c)). A similar pattern was observed on static fracture surfaces of amorphous metals after cathodic hydrogen charging.^[22,24,25,27,40] Its existence on the dynamic fracture surface of uncharged alloys may indicate the heterogeneous nucleation of local plastic deformation and propagation of the fracture front through microvoids. In addition, the high pressures developed in the material during cathodic hydrogen charging or laser shock may have similar effect on the failure characteristics.

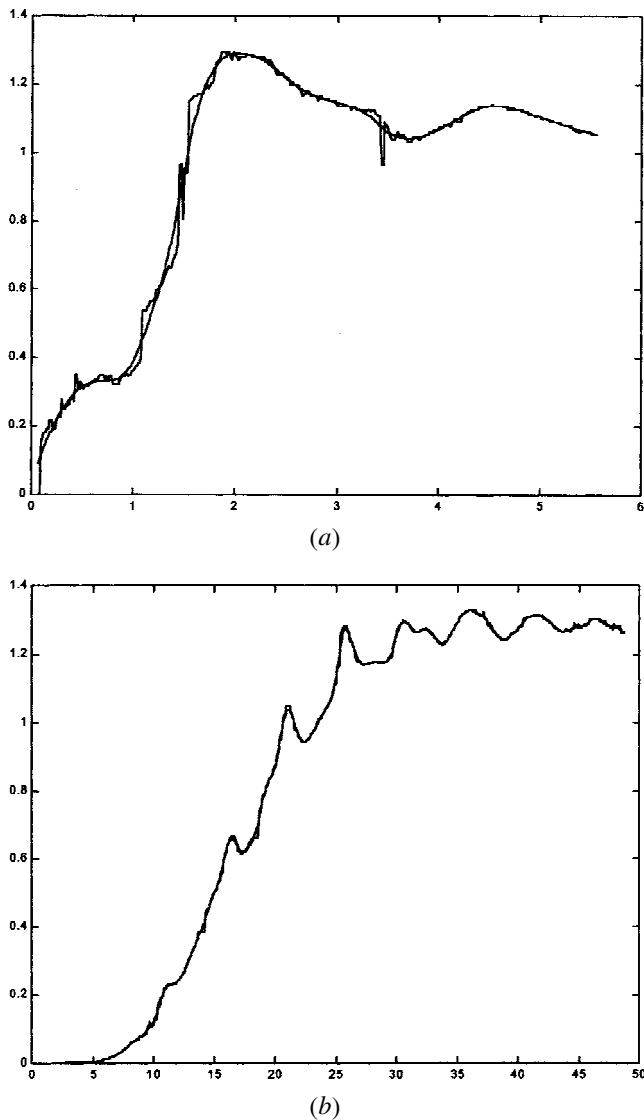
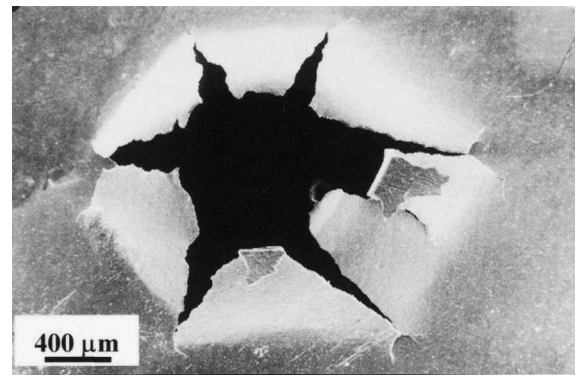


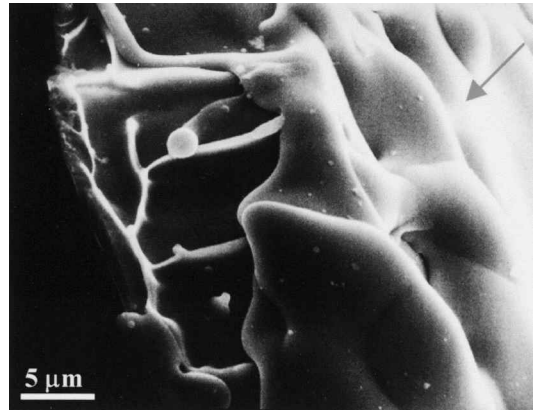
Fig. 4—(a) and (b) The free (rear) surface velocity as a function of time, corresponding to the interference patterns displayed in Fig. 3.

Figure 6 presents SEM micrographs from the hydrogenated amorphous alloy before (a) and after (b through d) laser shock. Before laser shock, one can notice voids on the surface preferably located along grinding scratches; in certain cases, the scratches have developed to cracks. After laser shock, the shape of the penetrating hole is macroscopically similar to that in the uncharged sample (Figure 6(b)). The fracture surface of the penetrating hole is mostly characterized by a combination of a smooth surface and vein pattern. Many voids, sometimes coalescing with one another, are observed near the fracture surface (Figure 6(c)). In addition, voids exist on the fracture surface itself (Figure 6(d)). Such findings may indicate the propagation of fracture through voids or *via* their coalescence.

The experimental results for uncharged pure crystalline iron, obtained using a laser pulse with a width of 2.2 ns, are summarized in Table II. At a strain rate of $3.5 \cdot 10^6 \text{ s}^{-1}$, an average spall strength of 1.9 GPa was measured. For comparison, the yield stress (σ_y) of pure iron under conditions of a strain rate of $8.3 \cdot 10^{-5} \text{ s}^{-1}$ is 50 MPa.^[41] It can be seen that the dynamic spall strength of the crystalline



(a)



(b)



(c)

Fig. 5—SEM micrographs of uncharged amorphous $\text{Fe}_{80}\text{B}_{11}\text{Si}_9$ alloy shocked by high-power laser: (a) spall morphology at the rear surface, (b) vein pattern (fractography) and front surface (indicated by arrow), and (c) cellular pattern (fractography).

metal is much higher than its static yield stress but similar to the dynamic spall strength of the iron-based amorphous alloy.

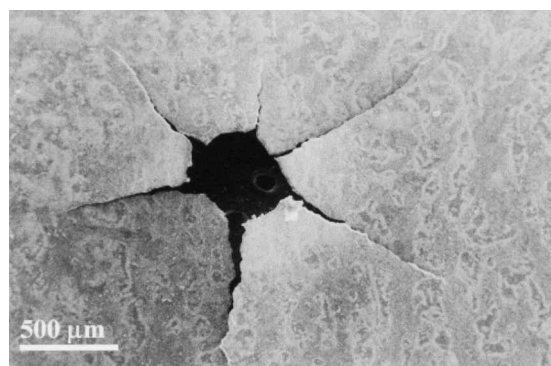
The theoretical spall strength of solids, P_{th} , considers interatomic interaction forces only and can be estimated^[42] from the cohesive energy per gram, U_{coh} , the normal density, ρ_0 , and the bulk modulus, B_0 :

$$P_{th} = \sqrt{\frac{U_{coh} B_0 \rho_0}{8}} \quad [6]$$

It is well known that P_{th} is about one order of magnitude



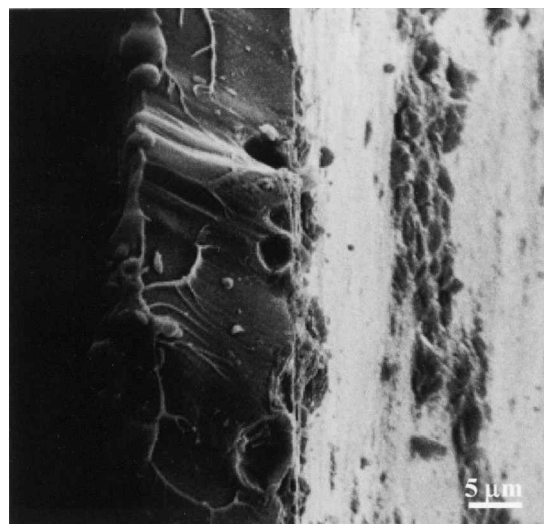
(a)



(b)



(c)



(d)

Fig. 6—SEM micrographs of charged amorphous $\text{Fe}_{80}\text{B}_{11}\text{Si}_9$ alloy, before and after laser shock: (a) surface before laser shock, (b) spall morphology at the rear surface, (c) voids coalescence near the fracture surface, and (d) vein pattern and voids on the fracture surface.

higher than the spall strength measured at strain rates in the range of 10^3 to 10^6 s^{-1} . This occurs due to the fact that the mechanical properties of solids are controlled by lattice imperfections that weaken the material. The strength of the material depends on the two following major factors.

- (1) The atomic structure (the interaction between atoms that compose the material) determines the crystalline structure and the theoretical strength.^[42]
- (2) Defects (voids in ductile materials, cracks in brittle materials, dislocations, inclusions, *etc.*) usually cause weakening of the material.

Typical distances between defects in materials are of the order of 10^{-2} to $10^0 \mu\text{m}$, whereas interatomic forces act for distance of the order of 10^0 \AA . Therefore, when high pressures are applied for very short times (*i.e.*, very high strain rates), the effect of defects in the crystalline structure is much less pronounced. At low strain rates, the strength of amorphous $\text{Fe}_{80}\text{B}_{11}\text{Si}_9$ is much higher than the strength of crystalline iron (in the absence of dislocations in the amorphous structure). On the other hand, at very high strain rates, there is not enough time for the action of the weakening mechanism *via* defects, and the strength of the material is mainly determined by the atomic structure and the strength of the interatomic bonds. Hence, at these conditions, the

spall strength of crystalline iron is similar to the one of the iron-based amorphous alloy. It should be noted that the values of the spall strength of crystalline iron (and of the amorphous alloy) are different from those of other crystalline metals such as aluminum and copper.^[6] This behavior supports the claim for significant effect of the atomic (and electronic) structure at very high strain rates. The significance of the electronic structure of iron-based amorphous alloys has recently been reported by Eliaz *et al.*^[43] with regard to hydrogen diffusivity and solubility as well.

Figure 7 presents the dependence of the spall strength of crystalline iron and amorphous $\text{Fe}_{80}\text{B}_{11}\text{Si}_9$ on strain rate, as measured in this work. Dekel *et al.*^[44] relate the rapid increase in the spall strength of the crystalline metal at strain rates of $\sim 10^7 \text{ s}^{-1}$ to a change in the spall mechanism. According to this attitude, at low strain rates, the spall is caused by the motion and coalescence of the initial flaws of the material (*e.g.*, dislocations). On the other hand, at high strain rates, there is not enough time for the flaws to move, and the spall is produced by the formation and coalescence of additional cavities where the interatomic forces become dominant. Material under tensile stress is in a metastable condition, and cavities of a critical radius are formed in it due to thermal fluctuations. These cavities grow

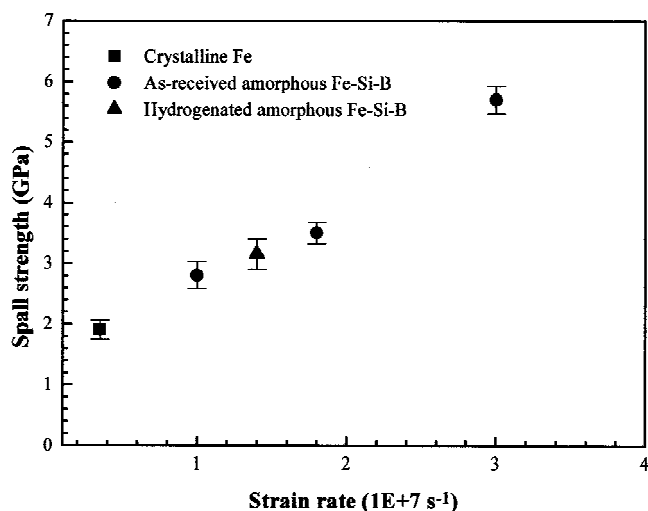


Fig. 7—Strain rate dependence of the spall strength of crystalline iron and amorphous Fe₈₀B₁₁Si₉.

due to the tension, and their total volume increases until the material disintegrates at the spall plane.

With regard to the traditional mechanisms generally used to explain the phenomenon of HE in crystalline metals and alloys, mechanisms of hydrogen interaction with dislocations^[10–14] are irrelevant to metallic glasses. In the case of amorphous alloys from the Fe-Si-B system, the hydride formation mechanism^[15,16] is irrelevant as well in the absence of hydride-forming elements. Filling of free volume by hydrogen atoms, a model specifically suggested for amorphous alloys (see, for example, Reference 27), seems to be inadequate for the explanation of HE in the amorphous Fe-Si-B alloy because failure of the ribbons occurred even in the absence of shear forces.^[28,30] The susceptibility of the amorphous Fe₈₀B₁₁Si₉ alloy to HE may be explained in terms of high-pressure bubble formation.^[17,28,30,45] According to this concept, microvoids that are introduced into the uncharged amorphous alloy during fabrication serve as preferred sites for recombination of hydrogen atoms. When the gas pressure inside these voids reaches a critical value, cracks might form and propagate between these voids even in the absence of external loads. The latter model is supported in the present work by

- (1) the identification of microvoids in the uncharged ribbon by SEM;^[28,30]
- (2) the identification of both larger voids and interconnecting cracks on the surface and in the cross section of charged ribbons;^[28,30]
- (3) the observation that these voids tend to form along scratches, introduced by the grinding process (Figure 6);
- (4) the identification of regions of cellular pattern on the fracture surfaces of charged ribbons;^[30]
- (5) the calculation, on the basis of thermal desorption spectroscopy, of a value of effective activation energy of hydrogen detrapping that is similar to that reported for hydrogen trapping in microvoids in crystalline metals;^[30] and
- (6) the predicted endothermic heat of solution for hydrogen in this alloy.^[30]

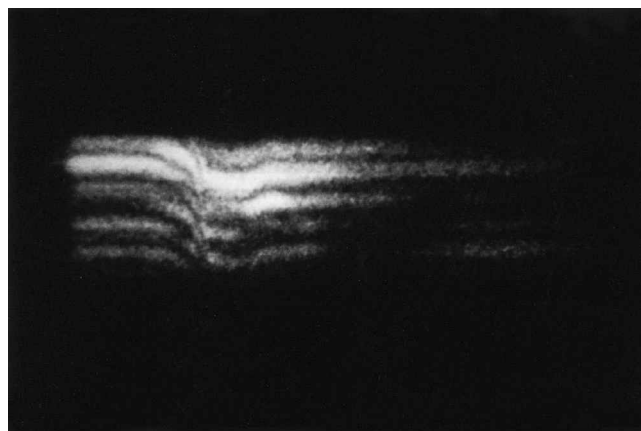


Fig. 8—The interference pattern of uncharged crystalline iron, obtained with ORVIS.

Yet, one still has to exclude the possibility of the dominance of the decohesion mechanism.^[9] This might be impossible by means of conventional experimental techniques. Fortunately, laser-induced shock wave measurements make it possible to distinguish between mechanisms that are insensitive to the strain rate (*e.g.*, decohesion) and mechanisms that do not have enough time to operate at very high strain rates (*e.g.*, growth of bubbles and propagation of interconnecting cracks). As previously explained in detail, at high strain rates, the strength of the material is determined mainly by the atomic structure and the strength of the interatomic bonds. Therefore, if the decohesion mechanism was the major one responsible for the HE phenomenon in the amorphous Fe-Si-B alloy, one would have expected the dynamic spall strength to decrease as a result of hydrogenation. However, because such a decrease in spall strength was not observed, we may assume that the decohesion mechanism is not significant in this case.

The interference pattern from uncharged crystalline iron (without acceleration while reverberation) is shown in Figure 8. The time scale is up to 5.6 ns, and the fringe constant is 0.301 km s⁻¹. It can be seen that the amplitude of the interference fringes during their shift is lower than that in the amorphous alloy. This means that the pullback velocity ($u_{\max} - u_{\min}$) is a larger fraction of the peak free surface velocity in the case of the amorphous alloy. The conversion of the interference pattern from Figure 8 to dimensions of free surface velocity *vs* time is displayed in Fig. 9.

Figure 10 presents SEM micrographs from the region of the penetrating hole that was formed after the severance of the spall layer in uncharged crystalline iron (laser pulse energy is 8 J and width is 2.2 ns). Both separation of material layers under the surface (Figure 10(c)) and cleavagelike fracture patterns (b and d) are observed.

V. CONCLUSIONS

1. Laser-induced shock wave measurements make it possible to distinguish between mechanisms of hydrogen embrittlement that are insensitive to the strain rate (*e.g.*, decohesion) and mechanisms that do not have enough time to operate at very high strain rates (*e.g.*, growth of bubbles and propagation of interconnecting cracks). The

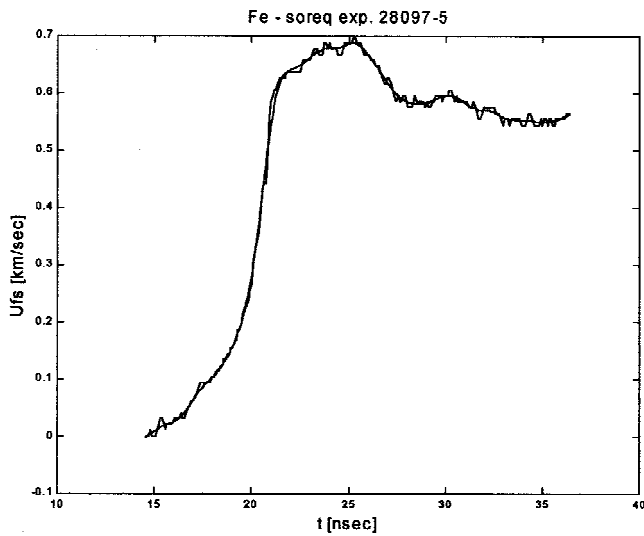


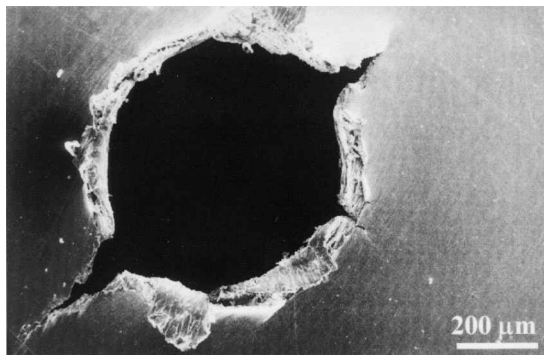
Fig. 9—The free (rear) surface velocity as a function of time, corresponding to the interference pattern displayed in Fig. 8.

absence of hydrogen effect on the dynamic spall strength of an amorphous $\text{Fe}_{80}\text{B}_{11}\text{Si}_9$ alloy was exploited in this research to support the mechanism of high-pressure bubble formation.

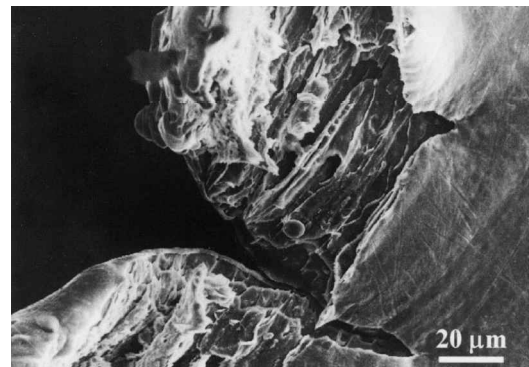
2. The presence of small regions of cellular pattern on the dynamic fracture surface of the uncharged amorphous

alloy may indicate the heterogeneous nucleation of local plastic deformation and propagation of the fracture front *via* microvoid coalescence. The observation of microvoids near and on the dynamic fracture surface of the charged amorphous alloy support this mechanism.

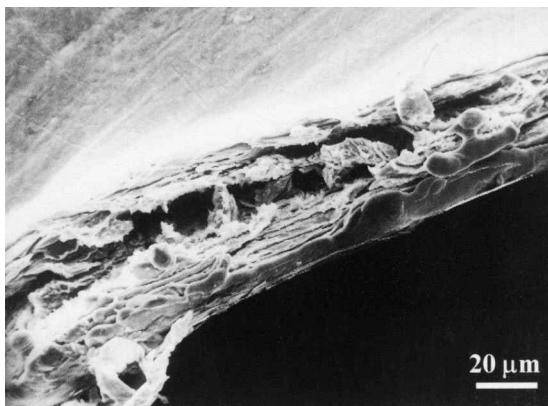
3. A cellular pattern is usually related to the static fracture of amorphous metals after cathodic hydrogen charging. Its presence in the dynamic spall strength of the uncharged amorphous alloy may, thus, indicate similar effects of the high pressures, which develop inside the material during cathodic hydrogen charging or laser-induced shock waves formation, on the characteristics of the fracture surface.
4. When high pressures are applied for very short times (*i.e.*, very high strain rates), the effect of defects in the crystalline structure is much less pronounced. At low strain rates, the strength of amorphous $\text{Fe}_{80}\text{B}_{11}\text{Si}_9$ is much higher than the strength of crystalline iron. On the other hand, at very high strain rates, there is not enough time for the action of the weakening mechanism *via* defects, and the strength of the material is mainly determined by the atomic structure and the strength of the interatomic bonds. Hence, at these conditions, the spall strength of crystalline iron is similar to the one of the iron-based amorphous alloy.
5. The unique macroscopic starlike shape of the dynamic fracture of an amorphous Fe-Si-B alloy probably results from the physical properties of the amorphous structure and not from the macroscopic embrittlement of this alloy.



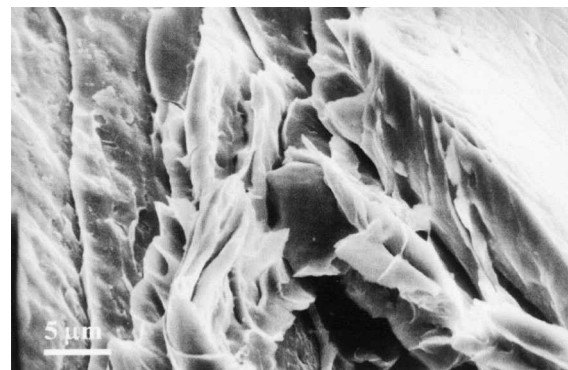
(a)



(b)



(c)



(d)

Fig. 10—(a) through (d) SEM micrographs of uncharged crystalline iron shocked by high-power laser.

ACKNOWLEDGMENTS

We thank Mr. E. Dekel for his contribution to the development of the theoretical and mathematical concept. We also thank Mr. S. Maman for his skillful technical assistance.

REFERENCES

1. G.E. Dieter: *Mechanical Metallurgy*, S.I. Metric, ed., McGraw-Hill Book Co., Singapore, 1988, pp. 496-99.
2. D.E. Grady and M.E. Kipp: in *High Pressure Shock Compression of Solids*, J.R. Asay and M. Shahinpoor, eds., Springer, New York, NY, 1993, pp. 265-322.
3. A.V. Bushman, G.I. Kanel, A.L. Ni, and V.E. Fortov: *Intense Dynamic Loading of Condensed Matter*, Taylor & Francis, Washington, DC, 1993.
4. D.D. Bloomquist and S.A. Sheffield: *J. Appl. Phys.*, 1983, vol. 54 (4), pp. 1717-22.
5. E. Moshe, E. Dekel, Z. Henis, and S. Eliezer: *Appl. Phys. Lett.*, 1996, vol. 69 (10), pp. 1379-81.
6. E. Moshe, S. Eliezer, E. Dekel, A. Ludmirsky, Z. Henis, M. Werdiger, I.B. Goldberg, N. Eliaz, and D. Eliezer: *J. Appl. Phys.*, 1998, vol. 83 (8), pp. 4004-11.
7. A.S. Tetelman and W.D. Robertson: *Trans. TMS-AIME*, 1962, vol. 224, pp. 775-83.
8. N.J. Petch and P. Stables: *Nature*, 1952, vol. 169, pp. 842-43.
9. W.J. Barnett and A.R. Troiano: *J. Metall. Trans. AIME*, 1957, vol. 209, pp. 486-94.
10. J.K. Tien, A.W. Thompson, I.M. Bernstein, and R.J. Richards: *Metall. Trans. A*, 1976, vol. 7, pp. 821-29.
11. P. Bastien and P. Azou: *Proc. World Metallurgy Congr.*, First American Society of Metals, Cleveland, OH, 1951, pp. 535-52.
12. A.N. Stroh: *Adv. Phys.*, 1957, vol. 6, pp. 418-65.
13. C.D. Beachem: *Metall. Trans.*, 1972, vol. 3, pp. 437-51.
14. D.S. Shih, I.M. Robertson, and H.K. Birnbaum: *Acta Metall.*, 1988, vol. 36 (1), pp. 111-24.
15. D.G. Westlake: *Trans. ASM*, 1969, vol. 62, pp. 1000-06.
16. H.K. Birnbaum: in *Hydrogen Effects on Material Behavior*, N.R. Moody and A.W. Thompson, eds., TMS, Warrendale, PA, 1990, pp. 639-60.
17. *Glassy Metals I*, H.-J. Gutherodt and H. Beck, eds., Springer-Verlag, Berlin, 1981.
18. S.R. Elliott: *Physics of Amorphous Materials*, 2nd ed., Longman Scientific & Technical, New York, NY, 1990.
19. *Amorphous Metallic Alloys*, F.E. Luborsky, ed., Butterworth and Co., London, 1983.
20. *Rapidly Solidified Alloys*, H.H. Liebermann, ed., Marcel Dekker Inc., New York, NY, 1993.
21. H.S. Chen: *Rep. Progr. Phys.*, 1980, vol. 43, pp. 353-432.
22. J.-J. Lin and T.-P. Perng: *Metall. Mater. Trans. A*, 1995, vol. 26A, pp. 197-202.
23. J.-J. Lin and T.-P. Perng: *J. Mater. Sci. Lett.*, 1991, vol. 10, pp. 1443-45.
24. T.K.G. Nambodhiri, T.A. Ramesh, G. Singh, and S. Sehgal: *Mater. Sci. Eng.*, 1983, vol. 61, pp. 23-29.
25. S. Ashok, N.S. Stoloff, M.E. Glicksman, and T. Slavin: *Scr. Metall.*, 1981, vol. 15, pp. 331-7.
26. A. Kawashima, K. Hashimoto, and T. Masumoto: *Scr. Metall.*, 1980, vol. 14, pp. 41-45.
27. H.W. Schroeder and U. Koster: *J. Non-Cryst. Solids*, 1983, vol. 56, pp. 213-18.
28. N. Eliaz, D. Eliezer, E. Abramoy, and E.J. Lavernia: *Proc. 3rd Pacific Rim Int. Conf. on Advanced Materials and Processing—PRICM3*, M.A. Imam, R. DeNale, S. Hanada, Z. Zhong, and D.N. Lee, eds., TMS, Warrendale, PA, 1998, vol. II, pp. 2757-64.
29. N. Eliaz and D. Eliezer: *Adv. Perf. Mater.*, 1999, vol. 6 (1), pp. 5-31.
30. N. Eliaz: Ph.D. Thesis, Ben-Gurion University of the Negev, Beer-Sheva, Israel, 1999.
31. J.B. Condon and T. Schober: *J. Nucl. Mater.*, 1993, vol. 207, pp. 1-24.
32. B. Arad, E. Moshe, S. Eliezer, E. Dekel, A. Ludmirsky, Z. Henis, I.B. Goldberg, N. Eliaz, and D. Eliezer: in *Shock Compression of Condensed Matter—1997*, S.C. Schmidt, D.P. Dandekar, and J.W. Forbes, eds., American Institute of Physics, New York, NY, 1998, pp. 459-62.
33. E. Moshe, A. Ludmirsky, E. Dekel, Z. Henis, I.B. Goldberg, S. Eliezer, N. Eliaz, and D. Eliezer: in *Physics and Mechanics of Finite Plastic and Viscoplastic Deformation*, A.S. Khan, ed., NEAT Press, MD, 1997, pp. 127-28.
34. K. Baumung and J. Singer: *Physics of Intense Light Ion Beams and Production of High Energy Density in Matter*, Forschungszentrum Karlsruhe GmbH, Karlsruhe, 1995, pp. 88-94.
35. L.M. Barker and K.W. Schuler: *J. Appl. Phys.*, 1974, vol. 45 (8), pp. 3692-93.
36. Z. Kaczkowski and H.S. Nam: in *Magnetic Properties of Amorphous Metals*, A. Hernando, V. Madurga, M.C. Sanchez-Trujillo, and M. Vazquez, eds., Elsevier Science, Amsterdam, 1987, p. 139.
37. *Technical Bulletin*, AlliedSignal, Parsippany, NJ, 1995.
38. L.A. Davis, S.K. Das, J.C.M. Li, and M.S. Zedalis: *Int. J. Rapid Solidif.*, 1994, vol. 8, pp. 73-131.
39. H. Rawson: *Properties and Applications of Glass*, Elsevier Scientific Publishing Company, Amsterdam, 1980, pp. 98-100.
40. M. Nagumo and T. Takahashi: *Mater. Sci. Eng.*, 1976, vol. 23, pp. 257-59.
41. *ASM Handbook*, vol. 2, *Properties and Selection: Nonferrous Alloys and Special-Purpose Materials*, ASM INTERNATIONAL, Materials Park, OH, 1990, pp. 1118-31.
42. D.E. Grady: *J. Mech. Phys. Solids*, 1988, vol. 3 (3), pp. 353-84.
43. N. Eliaz, D. Fuks, and D. Eliezer: *Acta Mater.*, 1999, vol. 47 (10), pp. 2981-89.
44. E. Dekel, S. Eliezer, Z. Henis, E. Moshe, A. Ludmirsky, and I.B. Goldberg: *J. Appl. Phys.*, 1998, vol. 84 (9), pp. 4851-58.
45. R.M. Latanision, C.R. Compeau, and M. Kurkela: in *Hydrogen Embrittlement and Stress Corrosion Cracking*, R. Gibala and R.F. Hehemann, eds., ASM, Metals Park, OH, 1984, pp. 297-313.